JGR Space Physics

RESEARCH ARTICLE
10.1029/2019JA026895

Plasma Flow in the North-South Aligned Discrete Aurora Equatorward of the Cusp

S. Taguchi[1,2], K. Hosokawa[3,4], and Y. Ogawa[5,6]

[1]Department of Geophysics, Graduate School of Science, Kyoto University, Kyoto, Japan, [2]Data Analysis Center for Geomagnetism and Space Magnetism, Graduate School of Science, Kyoto University, Kyoto, Japan, [3]Department of Communication Engineering and Informatics, University of Electro-Communications, Tokyo, Japan, [4]Center for Space Science and Radio Engineering, University of Electro-Communications, Tokyo, Japan, [5]National Institute of Polar Research, Tokyo, Japan, [6]Department of Polar Science, SOKENDAI (Graduate University for Advanced Studies), Kanagawa, Japan

Key Points:
- First simultaneous observations of north-south aligned discrete auroras equatorward of the cusp from an all-sky imager and EISCAT are presented
- A decrease in the elevated ion temperature is coincident with the north-south aligned aurora
- The plasma flow slows in the middle of the east-west dimension of the north-south aligned aurora

Correspondence to:
S. Taguchi,
taguchi@kugi.kyoto-u.ac.jp

Citation:
Taguchi, S., Hosokawa, K., & Ogawa, Y. (2019). Plasma flow in the north-south aligned discrete aurora equatorward of the cusp. *Journal of Geophysical Research: Space Physics*, *124*, 10,778–10,793. https://doi.org/10.1029/2019JA026895

Received 1 MAY 2019
Accepted 25 NOV 2019
Accepted article online 20 DEC 2019
Published online 30 DEC 2019

Abstract On the equatorward side of the dayside cusp there often appear diffuse auroras. In this paper, we report north-south aligned discrete aurora events and show the spatial relationships between the auroras and the plasma flow. Several events of the north-south aligned discrete auroral structures were identified using an all-sky imager at Longyearbyen, Svalbard, during the recovery of a moderately disturbed period on 8 December 2013. During a brief interval of the moderately disturbed period, the cusp shifted to higher latitudes; as a result, the field-aligned beam of the EISCAT Svalbard Radar (ESR) passed through the northern portion of the north-south aligned auroral structures. Simultaneous observations from the all-sky imager and ESR reveal that enhancements in ion temperature (caused by fast ion flow) occurred near the eastward and westward boundaries of the north-south aligned auroral structures. However, within the region of the most enhanced aurora, the ion temperature enhancements were moderately suppressed. These features indicate that the ion flow slows down in the region of electron precipitation responsible for north-south aligned auroral structures. We can quantitatively interpret the slowdown of the flow as the reduction of the electric field due to the polarization effect in the north-south aligned region of the increased Pedersen conductivity. It thus appears that the magnetospheric source of the north-south aligned discrete auroras is a limited area embedded in the region of plasma flow toward the dayside magnetopause.

1. Introduction

Early satellite imagery data from a line scanning radiometer sensitive to emissions between 400 and 1100 nm has shown that the dayside aurora consists of the diffuse aurora, discrete aurora, and the gap of the discrete auroras (e.g., Dandekar & Pike, 1978; Meng, 1981). When observed in a narrow band centered at a wavelength of 630 nm, the gap of the discrete auroras is not apparent; rather, the 630-nm auroras exhibit a continuous band across the midday sector of the auroral oval (Shepherd et al., 1976). Through later investigations using ground-based optical instruments, it has become clear that very dynamic auroras can be seen at the 630-nm wavelength in the midday sector, that is, the dayside cusp (e.g., Fasel, 1995; Lockwood et al., 1989; Sandholt et al., 1986; Sandholt & Farrugia, 2003; Taguchi et al., 2012, 2015a).

The dayside diffuse aurora appears continuously equatorward of the abovementioned dynamic cusp auroras and discrete auroras (e.g., Meng, 1981). This configuration is also supported by statistical analysis of the large amount of precipitating particle data from polar-orbiting spacecraft (Newell & Meng, 1992). The dayside diffuse auroras usually exist along the closed magnetic field lines threading either the central plasma sheet or the radiation belt in the magnetosphere. In the dayside diffuse auroras there sometimes appear auroral features that are either optically distinct from the diffuse auroras or completely separated from the higher-latitude discrete aurora and dynamic cusp aurora (see the review by Frey, 2007). Intriguing features of such auroras have been reported in a number of studies for about a quarter century (e.g., Chen et al., 2017; Elphinstone et al., 1993; Fuselier et al., 2004; Han et al., 2015, 2016, 2017; Hubert et al., 2003; Liou et al., 2002; Meng & Lundin, 1986; Rodriguez et al., 2012; Zhang et al., 2002, 2004; Zhang & Paxton, 2006).

The existence of the abovementioned auroras means that precipitation of the particles is enhanced in some limited areas in the dayside closed magnetic field line region. An important factor that can enhance particle

precipitation in this region is solar wind dynamic pressure. The importance of solar wind dynamic pressure in the rapid brightening of the persistent dayside auroral oval (e.g., Zhou & Tsurutani, 1999), as well as that for the large proton aurora brightness in the near-noon portion of the dayside auroral oval (e.g., Frey et al., 2003), has already been established. Zhang and Paxton (2006) reported three events of dayside auroral arcs that appeared on the equatorward side of the dayside auroral oval during intervals of high solar wind dynamic pressure. Two of the three events occurred when the solar wind dynamic pressure was extremely high, that is, 30–50 nPa, and the other event occurred during an interval of moderately high dynamic pressure, that is, ~7 nPa.

Using data from the SuperDARN radar, Zhang and Paxton (2006) also showed that the auroras are roughly aligned with the direction of the antisunward plasma flow. The results shown by these workers indicate that the distribution of the plasma flow can also be an important parameter for determining whether or not particle precipitation is enhanced in some limited regions in the midday sector. This importance can also be identified in the auroral photographs from an early study by Meng and Lundin (1986), who showed the radial configuration of the discrete aurora with fan-shaped arc structures that focus toward the cusp. We note that they categorized the midday auroral oval configuration into five types and that their illustration for Type 2 includes a very short north-south aligned discrete aurora near the equatorward edge of the auroral oval (their Figure 3). Using all-sky auroral image data and precipitating particle data from satellites, Rodriguez et al., (2012) reported that there exists a certain type of aurora that grows southward out from, and fading back into, the persistent midday aurora. They also found that the associated precipitating electron population shows features expected in the low-latitude boundary layer (LLBL). Han et al. (2015, 2016, 2017) examined a similar type of aurora and ascribed it to phenomenon in the open field line region; this is related to local enhancement of the dayside reconnection.

Although these previous studies suggest that discrete auroras appear along the antisunward plasma flow on the equatorward side of the cusp (where diffuse auroras are typically seen), the more detailed relationships between the region of antisunward plasma flow and enhanced electron precipitation causing the discrete aurora require clarification. In this study, we present aurora events that were identified as occurring during the intervals of low solar wind dynamic pressure and small negative IMF B_Z. We examine the relationship between auroral structures and plasma flow through simultaneous observations from an all-sky imager and the European Incoherent Scatter (EISCAT) Svalbard radar (ESR). The ESR has been used in many previous studies to understand the relationships between dayside auroras and plasma flow (e.g., Lockwood et al., 2000; Moen et al., 2008; Oksavik et al., 2004; Skjæveland et al., 2017; Taguchi et al., 2015b, 2017). To our knowledge, this is the first work to focus on discrete auroral structures equatorward of the cusp, where diffuse auroras are usually seen, using simultaneous observations obtained by an all-sky imager and the ESR.

2. Ground-Based Instrumentation

The ground-based instrumentation used in this study consists of an all-sky imager and the ESR. The all-sky imager is equipped with an electron multiplier charge-coupled device camera (Hamamatsu, C9100-13) with an imaging resolution of 512 × 512 pixels. This imager has been operating in Longyearbyen, Svalbard (geographical latitude: 78.1°N, longitude: 16.0°E), since October 2011 (Taguchi et al., 2012). MLT at Longyearbyen is approximately 3 hr ahead of UT. In the present study, we focused on an event that took place on 8 December 2013. Three types of image data are available for that winter season: 557.7-nm data obtained every 1 min with an exposure time of 2 s; 630.0-nm data obtained every 4 s with an exposure time of 4 s; and 630-nm data obtained five times per minute with a 1-s exposure time (Taguchi et al., 2015a, 2015b). We analyzed all three types of image data. One of the three types, the 630.0-nm data obtained every 4 s with an exposure time of 4 s, is useful not only for the study of auroras but also for the study of polar cap patches whose emissions are weaker than those of the aurora (Hosokawa et al., 2013; Hosokawa et al., 2013; Hosokawa et al., 2016a, 2016b; Sakai et al., 2014). For the ESR, we used data from a fixed 42-m dish antenna. The dish antenna is fixed so that its beam is aligned with the magnetic field lines above the ESR site.

3. Observations

3.1. Observations from 8 December 2013

Figure 1 shows the 630-nm aurora overviews in a keogram format for 0700–1100 UT on 8 December 2013, together with the *SYM-H* index (Iyemori & Rao, 1996) and the *AL* index. The aurora intensified at ~0725

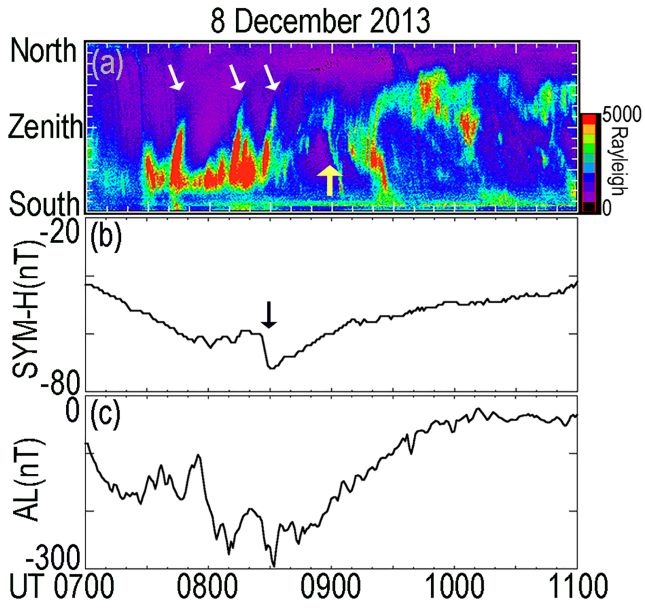

Figure 1. (a) The 630.0-nm auroral intensity in the north-south keogram for 0700–1100 UT on 8 December 2013, (b) *SYM-H* index, and (c) *AL* index. The white arrows in Figure 1a indicate the poleward moving auroras in the cusp, and the yellow arrow indicates the observation of the north-south aligned auroral structure examined in this study. The black arrow in Figure 1b represents the sharp decrease in the *SYM-H* index, that is, SI^{-}.

UT and clear poleward-moving aurora features were seen subsequently at ~0745, ~0815, and ~0830 UT (white arrows in Figure 1a). Immediately after 0830 UT, the auroras dimmed suddenly and almost simultaneously the negative sudden impulse SI^{-} (e.g., Araki, 1994) occurred (Figure 1b); the black arrow in the figure indicates SI^{-}. The *SYM-H* index started to decrease sharply at 0827 UT, reaching −72 nT at 0830 UT. The concurrence of SI^{-} and a reduction of auroral intensity has been reported previously by Liou et al. (2006), who ascribed the sudden reduction of auroral intensity to a sharp decrease in the solar wind dynamic pressure. Similarly, we can infer that a sharp decrease in the solar wind dynamic pressure, which is the cause of SI^{-}, hit the dayside magnetopause immediately before 0827 UT. In fact, solar wind dynamic pressure data obtained upstream in the solar wind shows a sharp decrease at ~0730 UT, which will be discussed later.

Figure 1a also shows that the equatorward boundary of the aurora shifted gradually poleward after the interval of the poleward moving auroras. At ~0855 UT, the equatorward boundary, defined as having an intensity of > 2,000 *R*, was situated near the zenith. This boundary generally coincides with the open/closed field line boundary (Milan et al., 1999; Taguchi et al., 2015a). It thus appears that the open/closed boundary in the north-south meridian is located near the zenith, that is, 75–76° MLAT at 0855 UT.

The yellow arrow in Figure 1a indicates the north-south aligned auroral structure examined in this study. In the keogram format, the auroral structures appear to be extending southward until ~0905 UT; however, this "slope" in the keogram does not show that the aurora moved southward. As is shown later, the southern portion of the north-south aligned auroral structures tilted slightly eastward. This tilting auroral form passed through the north-south meridian by moving to the west, producing the slope in the north-south keogram. Figure 1c shows the *AL* index. During the period 0855–0905 UT, this index varied from −214 to −151 nT. This increase indicates that the north-south aligned auroral structures occurred during the recovery of a moderately disturbed period.

At around 0905 UT, auroras near the zenith were enhanced and a similar "slope" can be seen between ~0910 and ~0930 UT. This slope occurred at lower latitudes than the slope at ~0900 UT and it is the persistent dayside aurora, rather than the north-south aligned aurora, that was present near the zenith. This indicates that the ESR's beam, which is close to the zenith, passes through the persistent dayside aurora and not the north-south aligned aurora structures equatorward of the persistent dayside aurora. In section 3.2 we present the ESR data obtained before ~0905 UT to explain the characteristics of the north-south aligned aurora structures.

Figure 2 shows examples of the all-sky image data obtained in the near-noon MLT sector. Figures 2a and 2b are the 557.7- and 630.0-nm images of an event of the poleward-moving cusp aurora, which was observed at 0745:33 and 0745:50 UT, respectively. Figure 2c shows the 557.7-nm image of the aurora obtained at 0859:38 UT. The aurora structures were generally north-south aligned. The north-south aligned feature is more evident in the 630.0-nm image (Figure 2d), which was obtained immediately after the 557.7-nm image. The southern portion of the structures extended in the direction of low-elevation angles. We note that the emission along the southern boundary of the imager's field of view in Figures 2c and 2d is simply due to faint light from the Sun beneath the horizon, rather than from the auroral emission.

The northern boundary of the north-south aligned auroral structures is not clearly identified in the 630.0-nm image (Figure 2d) because the 630.0-nm cusp aurora is brightened in a large region immediately to the north of the north-south aligned auroral structures. In Figures 2c and 2d, several other elongated auroral structures are seen in the southeastward direction; these are a similar type of the north-south aligned auroral structures. We will discuss this briefly in section 3.2.

The poleward moving cusp aurora (Figures 2a and 2b) shows that the auroral emissions at 630.0 nm were much stronger than those at 557 nm. The black diamond in each image of Figure 2 indicates the direction

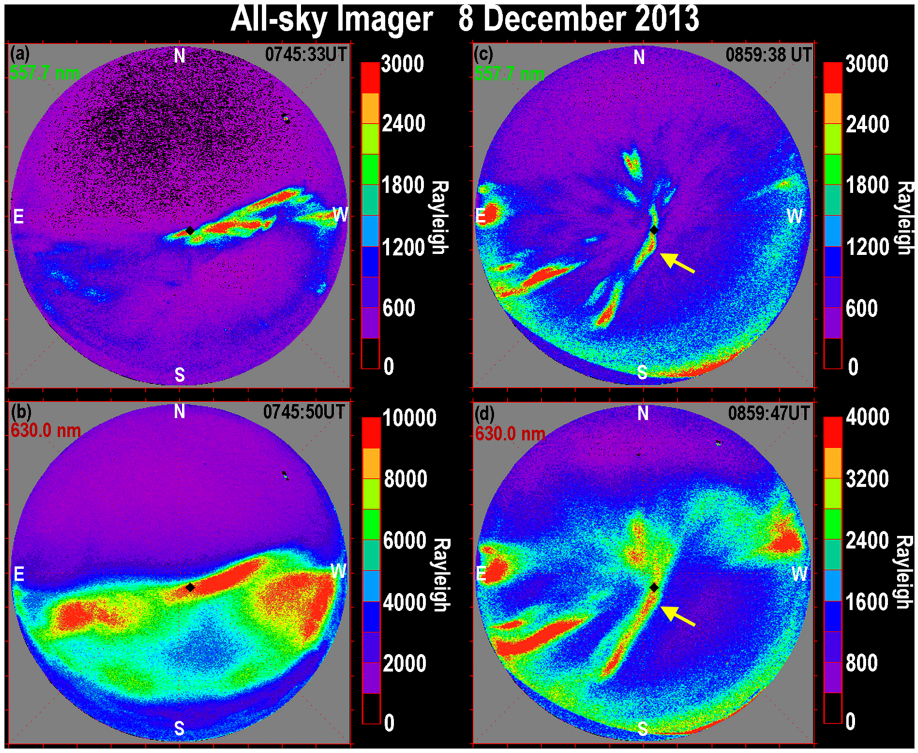

Figure 2. (a) The 557.7-nm all-sky image taken at 0745:33 UT, (b) 630.0-nm image at 0745:50 UT, (c) 557.7-nm image at 0859:38 UT, and (d) 630.0-nm image at 0859:47 UT on 8 December 2013. A black diamond in each figure shows the magnetic zenith at Longyearbyen, and this is also the direction of the ESR field-aligned radar beam. N-S and E-W represent the geomagnetic north-south and east-west, respectively. The yellow arrows in Figures 2c and 2d indicate the north-south aligned auroral structures examined in this study.

of the tangent to the magnetic field lines at Longyearbyen, that is, the magnetic zenith at Longyearbyen. The auroral intensities in a single pixel pointing to the magnetic zenith were 10,610 *R* at 630 nm (Figure 2b) and 710 *R* at 557.7 nm (Figure 2a). The intensity ratio of 557.7 and 630.0 nm is indicative of the energy of the incoming electrons. The ratio of 557.7-nm intensity to 630.0-nm intensity was very low, that is, 0.067 (710 *R*/1,0610 *R*). A low ratio is typical for strong cusp auroras, which can be explained as being a result of electrons precipitating along open field lines (e.g., Lorentzen & Moen, 2000). In the image shown in Figure 2b, the clear equatorward boundary of strong 630.0-nm emissions is located at much lower latitudes than the magnetic zenith, showing a smooth curve from east to west. Taking into account a recent study on the comparison between the 630-nm image from our all-sky imager and the precipitating cusp particles observed by a polar-orbiting satellite (Taguchi et al., 2015a), it can be stated that this boundary was close to the open/closed boundary at this time.

The north-south aligned auroral structures had intensities of 2,760 and 3,660 *R* near the magnetic zenith (black diamond in Figures 2c and 2d) at wavelengths of 557.7 and 630.0 nm, respectively. The ratio of the former to the latter was 0.75 (2,760 *R*/3,660 *R*), that is, more than 10 times larger than that of the poleward moving cusp aurora. In addition, we calculated the auroral intensity ratio using data for a larger area (25 pixels) around the magnetic zenith and those for a longer period (50 s). We chose 50 s based on the possible lifetimes of the O(^1D) state (30–80 s) at 250–300 km (e.g., Sipler & Biondi, 1972). Table 1 summarizes the results of the comparison between the intensity ratio for the poleward-moving cusp aurora and that for the north-south aligned aurora.

The ratio of the poleward moving cusp aurora was between 0.067 and 0.13, whereas the ratio for the north-south aligned aurora ranged from 0.73 and 1.1. The north-south aligned aurora had a much larger ratio than the poleward moving cusp aurora regardless of whether the data were derived from a single pixel, a larger area, or a longer period of time. These 557.7/630.0 intensity ratios for the north-south aligned aurora are

Table 1
The 557.7 nm/630.0 nm Emission Intensity Ratio

	Moving cusp aurora	N-S-aligned aurora
$I_{557.7}/I_{630.0}$	0.067 (= 710 *R*/10,610 *R*)	0.75 (= 2,760 *R*/3,660 *R*)
$I_{557.7}$/50-s averaged $I_{630.0}$	0.081 (= 710 *R*/8,720 *R*)	1.1 (= 2,760 *R*/2,540 *R*)
$I^*_{557.7}/I^*_{630.0}$	0.1 (= 1,040 *R*/10,050 *R*)	0.73 (= 2,460 *R*/3,360 *R*)
$I^*_{557.7}$/50-s averaged $I^*_{630.0}$	0.13 (= 1,040 *R*/8,260 *R*)	0.98 (= 2,460 *R*/2,510 *R*)

Note. I^* represents the intensity averaged over 5 × 5 pixels around the pixel pointing the magnetic zenith.

consistent with ratios indicating a plasma sheet origin source (e.g., Lorentzen & Moen, 2000). We thus infer that the north-south aligned auroral structures (Figures 2c and 2d) occurred in the closed field line region.

Figure 3a shows a close-up view of the 630-nm north-south aligned aurora (shown in Figure 2d) projected onto an Earth-centered sphere at a height of 250 km and with a background of MLT and MLAT coordinates. We used the altitude adjusted corrected geomagnetic coordinates (Baker & Wing, 1989). The yellow arrow indicates the north-south aligned aurora examined in this paper. For this auroral structure, a relatively strong intensity (>3,200 *R*) occurred, mostly between ~73° and ~75°. Other relatively strong auroras (red color) are also seen at latitudes lower than 76° both on the prenoon and postnoon sides. The white line indicates the trajectory of the DMSP F16 spacecraft, whose altitude was ~835 km. The spacecraft passed through the region poleward of the north-south aligned aurora. Immediately before 0858 UT, the spacecraft passed the 1200 MLT meridian.

Figure 3b shows SuperDARN convection contours and estimated fitted map potential velocity vectors for 0900–0902 UT. The velocity vectors indicate that the plasma convection over Svalbard is generally northwestward, which is almost parallel to the north-south aligned aurora. It appears that the plasma convection becomes more northward at higher latitudes in the prenoon sector.

The horizontal ion flow having a northward component in such a prenoon sector can also be seen in the data obtained from the ion drift meter of the DMSP F16 spacecraft (Greenspan et al., 1986). Figure 4 shows the data for 0850–0905 UT on this day. The ion drift data indicate that the drift had generally northward (antisunward) components in the prenoon polar cap, although drift with weak sunward components occurred around 1200 MLT (~0858 UT). The drift data also indicate that the prenoon convection reversal was located at ~76.0° MLAT, although there was a very brief interval of the flow with antisunward components on its equatorward side. Considering that convection reversal in the prenoon sector generally occurs within the LLBL region (e.g., Newell et al., 1991), the open/closed boundary should occur near this convection reversal, that is, ~76.0° MLAT.

Figure 5 shows the solar wind and IMF data obtained upstream in the solar wind by the ACE spacecraft, together with the *SYM-H* index, for 0000–1200 UT on 8 December 2013. During this interval, the ACE spacecraft was positioned at $X \sim 233\ R_E$ in the Geocentric Solar Magnetospheric coordinate system (GSM). No time lag is considered in the ACE data plot. The black triangle at the bottom of Figure 5 indicates the time of the all-sky image data shown in Figure 2d (0859:47 UT). Figures 5a–5c show the X_{GSM}, Y_{GSM}, and Z_{GSM} components, respectively, of the IMF data (16-s average). The Z_{GSM} component, B_Z, (Figure 5c) took positive values between ~0645 and ~0710 UT but then became negative until ~1100 UT. Figure 5b shows that after ~0730 UT, the Y_{GSM} component, B_Y, was of relatively small magnitude compared with before 0730 UT. The X_{GSM} component of the IMF, B_X, was predominantly negative (Figure 5a) after ~0730 UT. Figure 5d shows the IMF clock angle, defined as $\tan^{-1}(B_Y/B_Z)$. The two horizontal dashed lines (135° and 225°) indicate the range of negative B_Z and $|B_Z| \geq |B_Y|$. During ~0730 to ~1100 UT, the clock angle was within this range (except for several brief intervals). Figure 5e shows the IMF cone angle, defined as $\cos^{-1}(B_X/B_T)$, where B_T is the total magnitude of the IMF. During the above time interval, the cone angle changed dramatically between ~0° and ~90°.

The solar wind proton density, solar wind speed, and solar wind dynamic pressure (64-s average data) are shown in Figures 5f–5h, respectively. The solar wind proton density was measured as a constant ~2.7 cm^{-3} (average for 0730–0830 UT) after a sharp decrease at 0730 UT. The solar wind speed increased sharply at this time, exhibiting a constant value of ~620 km/s (average for 0730–0830 UT). The solar wind dynamic pressure (Figure 5h) calculated from these two parameters also took stable values, that is, ~1.9 nPa (average for

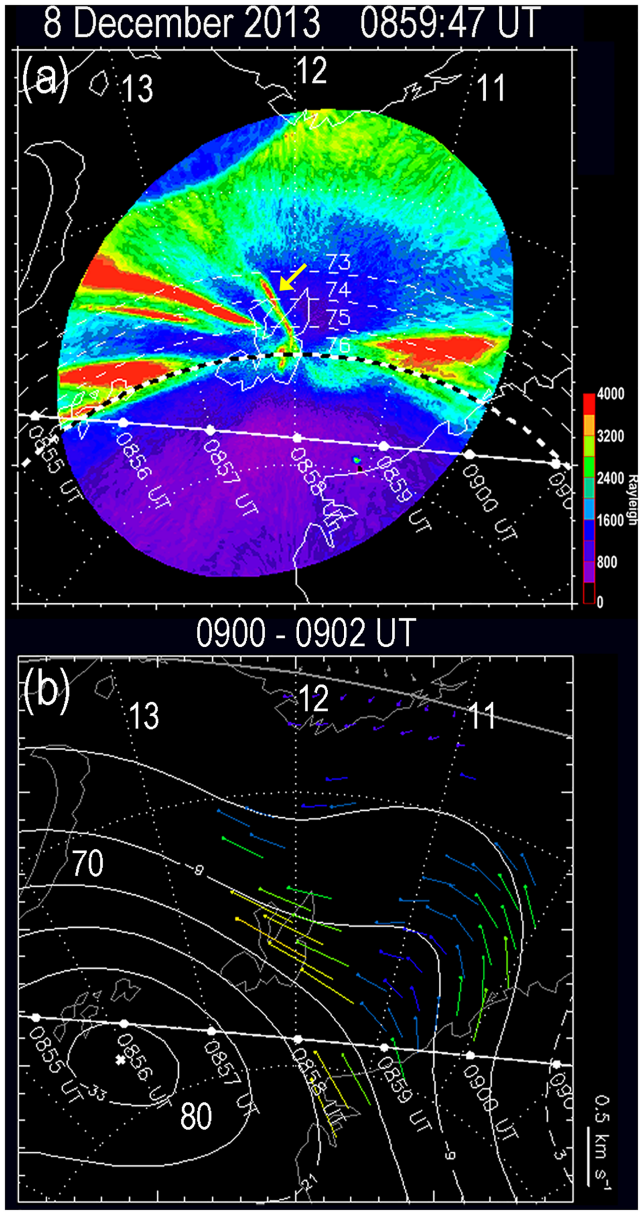

Figure 3. (a) The 630.0-nm auroral image at 0859:47 UT, and (b) SuperDARN convection contours and estimated fitted map potential velocity vectors for 0900–0902 UT, projected on the magnetic latitude and magnetic local time coordinate system. The yellow arrow in Figure 3a indicates the north-south aligned aurora examined in this study. The black and white dashed line represents 76° MLAT. The trajectory of the DMSP F16 spacecraft approximately between 0855 and 0901 UT is shown with the while line.

0730–0830 UT). As stated earlier, a sharp decrease in the solar wind dynamic pressure occurred at 0730 UT. The time delay of SI^{-} at 0827 UT from the sharp decrease in the solar wind dynamic pressure at 0730 UT is 57 min.

This delay time indicates that the solar wind observed by ACE at ~0803 UT (= 0900 UT − 57 min) reached the dayside magnetopause at ~0900 UT, when the auroras shown in Figures 2c and 2d were obtained. The ACE observation at ~0803 UT was much later than the time at which B_Z became slightly negative (0710 UT; Figure 5c). Relatively small negative B_Z values were sustained from 0710 to 1100 UT. We can infer that the IMF existed with a small negative B_Z component near the dayside magnetopause at ~0900 UT. This is consistent with the DMSP F16 observation (Figure 4), which shows that the ion drift was predominantly antisunward in the dayside polar cap. We can also infer that the solar wind dynamic pressure and solar wind speed at that time were ~2 nPa and ~620 km/s, respectively. However, it should be noted that the solar wind density and dynamic pressure were extremely high (~40 cm^{-3} and ~18 nPa, respectively) immediately before 0200 UT and that the relatively high densities (>10 cm^{-3}) at the ACE position continued until ~0520 UT.

3.2. Simultaneous Observations From the All-Sky Imager and the ESR

Before showing detailed data for the brief period when the ESR observed the north-south aligned auroral structures, we present the general plasma features obtained by the ESR between 0700 and 1100 UT. Figure 6 shows the 32-s integrated electron density (N_e), electron temperature (T_e), ion temperature (T_i), and field-aligned component of ion velocity ($V_{i//}$) measured by the ESR. Figure 6a presents the height profiles of N_e. The N_e at 300- to 400-km altitude was enhanced many times during the plotted interval. Some of the N_e enhancements (e.g., the first enhancement at ~0745 UT) were accompanied by high T_e values (Figure 6b), whereas others (e.g., the second enhancement at ~0802 UT) were not.

The two events appeared during the interval when the dayside main auroral emissions occurred at lower latitudes than the direction of the zenith (Figure 1a). As shown in Figure 1a, a poleward-moving cusp aurora passed through the vicinity of the zenith at ~0745 UT (white arrow). The N_e enhancements accompanied by high T_e at ~0745 UT were likely caused by electron precipitation associated with the poleward moving cusp aurora. In contrast, similar auroral features were not seen near the zenith at ~0802 UT (Figure 1a), indicating that high-density plasma was transported to that region (but not produced there via electron precipitation). The T_i data (Figure 6c), which reflect horizontal ion flow (e.g., St. Maurice & Hanson, 1982), showed clear enhancements both at ~0745 and ~0802 UT, suggesting that high-density plasmas were fast flowing at these times. The ion upflow data (Figure 6d) show a clear difference between these two events. At ~0745 UT, ion upflow was prominent at altitudes > 400 km (pinkish color in Figure 6d), whereas ion upflow was not clear during the ~0802 UT event. The ion upflow coincident with cusp electron precipitation is consistent with results from previous studies (e.g., Ogawa et al., 2003).

The black triangle at the bottom of each panel in Figure 6 indicates the time at which the auroral image shown in Figure 2d was obtained (0859:47 UT). When the north-south aligned auroral structures were observed, N_e was enhanced at altitudes down to ~150 km (Figure 6a). At altitudes of ~300 km, T_e and T_i

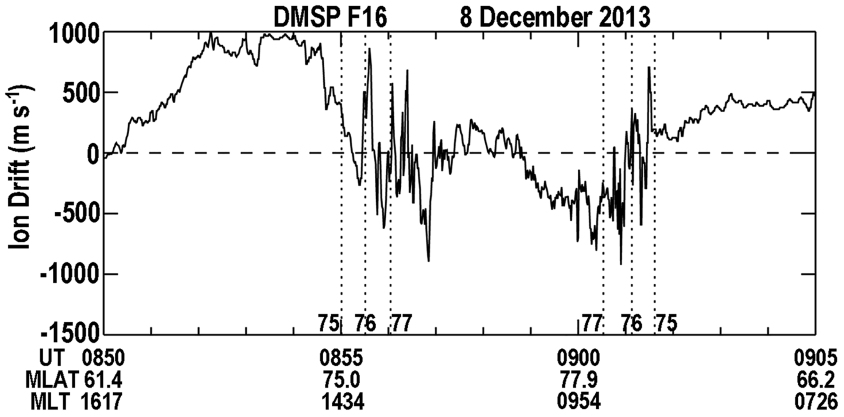

Figure 4. Sunward component of the ion drift observed by DMSP F16 for 0850–0905 UT on 8 December 2013. The three vertical dotted lines on the left indicate the times at which DMSP passed through 75°, 76°, and 77° MLAT in the postnoon sector, and the three lines on the right show the times at which the spacecraft passed through 77°, 76°, and 75° MLAT in the prenoon sector.

showed sharp increases slightly earlier than did N_e. Ion upflow was not prominent at this time but became clear several minutes later.

Figure 7 shows the expanded T_i and N_e plots for a 10-min period (0853–0903 UT), with the plot of the auroral intensities in the direction of the ESR's field of view. Figure 7a presents the variations in the auroral intensities at 557.7 and 630.0 nm. The maximum values for the 557.7- and 630.0-nm emissions are 2,760 *R* and 3,360 *R*, respectively, as shown in Table 1. Figure 7b shows the variations in average T_i from a 150-km width centered at 275 km (i.e., 200 to 350 km), which is a typical *F* region height where atomic oxygen is the main neutral species. Figure 7c presents the variations in the average N_e from the lower altitudes (i.e., 150–200 km), which may be an indicator of the existence of relatively high-energy electron precipitation.

At around Time 1 (0856:56 UT), one of the times at which 630-nm auroral images were obtained, T_i was not yet clearly enhanced. T_i started to become enhanced at around Time 2. At Time 3, the 630-nm auroral intensity was approximately 1,350 *R*, that is, similar to the values at Times 1 and 2. The 557.7-nm auroral intensity was not enhanced during Times 1–3, when T_i was increasing. From Times 3 to 5, variations in the 630.0-nm auroral intensity and T_i were anticorrelated. T_i reached a maximum of ~1900 K near Time 3 and a minimum of ~1400 K around Time 4, that is, a depression of ~500 K. The auroral intensity recorded a maximum of 3,660 *R* near Time 4. Hence, the T_i enhancement was suppressed when the 630-nm auroral intensity was high. A similar relationship was observed between T_i and the 557.7-nm auroral intensity. The N_e value at altitudes of 150–200 km was clearly enhanced when T_i enhancement was suppressed (Figure 7c), suggestive of the occurrence of relatively high-energy electron precipitation.

A second T_i maximum occurred at Time 5. At Time 6 (0901:13 UT), the 630.0-nm auroral intensity was ~1,900 *R* and T_i was ~1400 K, dropping to background levels (~1100 K) approximately 90 s later. The auroral intensity continued to exhibit values of 1,900 ± 100 *R* until 0901:35 UT. We took this UT to be the end of the auroral enhancement and estimated the duration of the auroral enhancement to be ~170 s (0858:47 to 0901:35 UT). We will show later that the choice of this UT (Time 6) as the end time is reasonable because the auroral intensity at Time 5 still comes from the north-south aligned auroral structures.

Figures 8a–8f show the placement of the north-south aligned auroral structures observed at 630.0 nm relative to the direction of the ESR beam at Times 1–6, respectively. The format of each all-sky image is the same as that of the image shown in Figure 2d. Figure 8a presents the image obtained at Time 1. The north-south aligned auroral structure (yellow arrow) existed on the eastward side (left side in the figure) of the ESR beam (black diamond). The north-south aligned auroral structures still existed on the eastward side of the ESR beam at Time 2 (Figure 8b), when the ESR observed a sharp increase in T_i (Figure 7b). Comparing the image in Figure 8b with the image at Time 1 (Figure 8a), the north-south aligned auroral structures moved westward such that the ESR beam at Time 2 passed through the region closer to the auroral structures than it

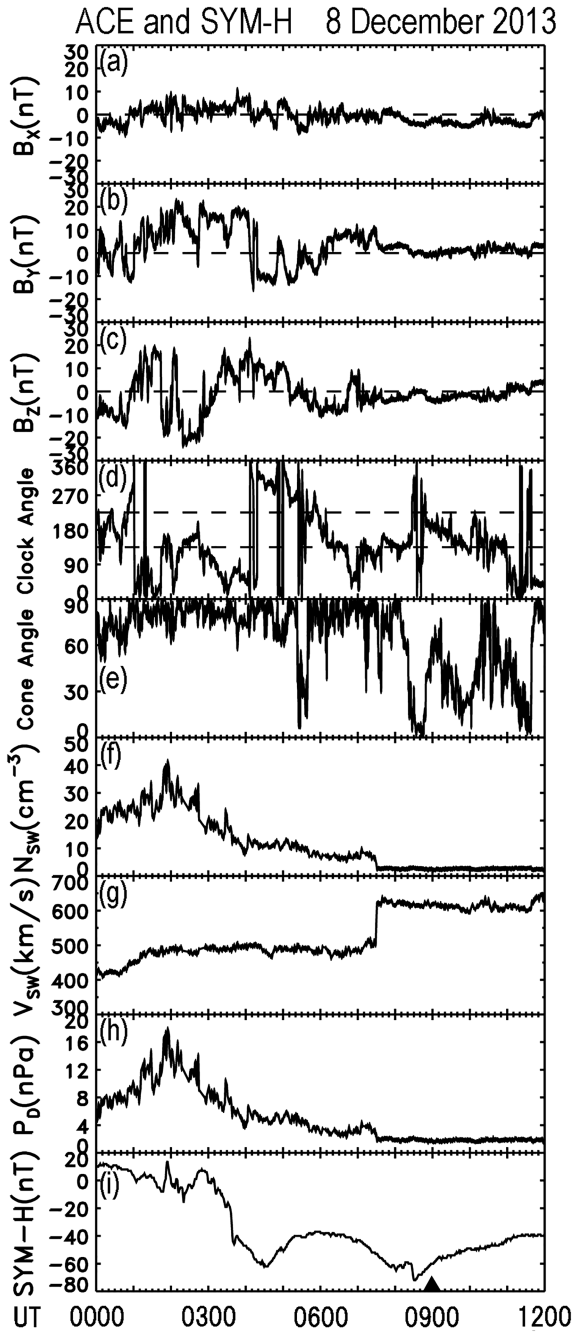

Figure 5. Solar wind and IMF observed by the ACE spacecraft and the *SYM-H* index for 0000–1200 UT on 8 December 2013. The *X*, *Y*, and *Z* components of the IMF in the Geocentric Solar Magnetospheric coordinate system are plotted in (a), (b), and (c), respectively. IMF clock angle and cone angle are plotted in (d) and (e), respectively. The solar wind proton density, speed, and dynamic pressure are shown in (f), (g), and (h), respectively. The plot in (i) represents the *SYM-H* index. The black triangle indicates the time of the all-sky image shown in Figure 2d (0859:47 UT).

did at Time 1. The ESR beam at Time 3 passed through the region closer to the auroral structures (Figure 8c) than it did at Time 2 because of the westward movement of the auroral structures. As shown in Figure 7b, Time 3 represents the maximum ESR T_i. Fast ion flow, which is responsible for high T_i values, existed near the westward boundary of the north-south aligned auroral structures (Figure 8c).

The general shape of the north-south aligned auroral structures did not change substantially from Time 1 (Figure 8a) to Time 3 (Figure 8c). Based on the 630.0-nm auroral intensity variations (>1,800 *R*) along the east-west plane containing the ESR's beam direction, the east-west width of the north-south aligned auroral structures at Time 3 was ~30 km at an altitude of 250 km. Because it takes 170 s for the 30-km-wide region to pass through a fixed point (Figure 7a), the westward speed can be estimated as ~0.18 km/s.

Comparing the image in Figure 8c with those in Figures 8a and 8b, the aurora that extended on the poleward side of the north-south aligned auroral structures, thought to be the cusp aurora, did not show any significant enhancements at Time 3 when the maximum T_i was observed. This implies that the fast ion flow, inferred to be located near the westward boundary of the north-south aligned auroral structures at Time 3, was not caused by a transient process associated with cusp aurora brightening.

Figure 8d shows the all-sky image at Time 4, at which time the auroral intensity in the direction of the ESR beam was at its maximum (Figure 7a). Comparing Figure 8d with Figure 8c, we consider that the higher auroral intensity at Time 4 compared with Time 3 (Figure 7a) reflects the passage of the moving auroral structures through the direction of the ESR beam at Time 4. We also know from Figure 8d that the maximum auroral intensity was recorded in the middle of the east-west dimension of the north-south auroral structures, where the suppression of T_i enhancements was also observed (Figure 7b). The cusp aurora, located on the northern side of the north-south aligned auroral structures, did not show any suppressed features at Time 4 (Figure 8d).

Figure 8e represents the image at Time 5. The ESR's field of view passed through the vicinity of the eastward boundary of the north-south aligned auroral structures. T_i was recorded as being close to the maximum T_i (around Time 3). The T_i value suggests that ion flow near the eastward boundary of the north-south aligned auroral structures was similar to that near the westward boundary. Figure 8f shows the all-sky image at Time 6. At this time, the ESR's field of view passed through the northeastward edge of the north-south aligned auroral structures, although a small horn-like structure appeared nearby. The ESR T_i in this direction was ~1400 K (Figure 7b), which is greater than the background level for this event (~1100 K).

A few other elongated auroral structures were observed in the southeastward direction on the eastward side of the north-south aligned auroral structure throughout Times 1–6 (Figures 8a–8f). After Time 6, these auroral structures moved further westward and then passed through the north-south median in the imager's field of view. The passage can be clearly seen in the north-south keogram in Figure 1a, for example, after ~0910 UT. As stated in section 3.1, the ESR's field of view did not pass through these auroral structures.

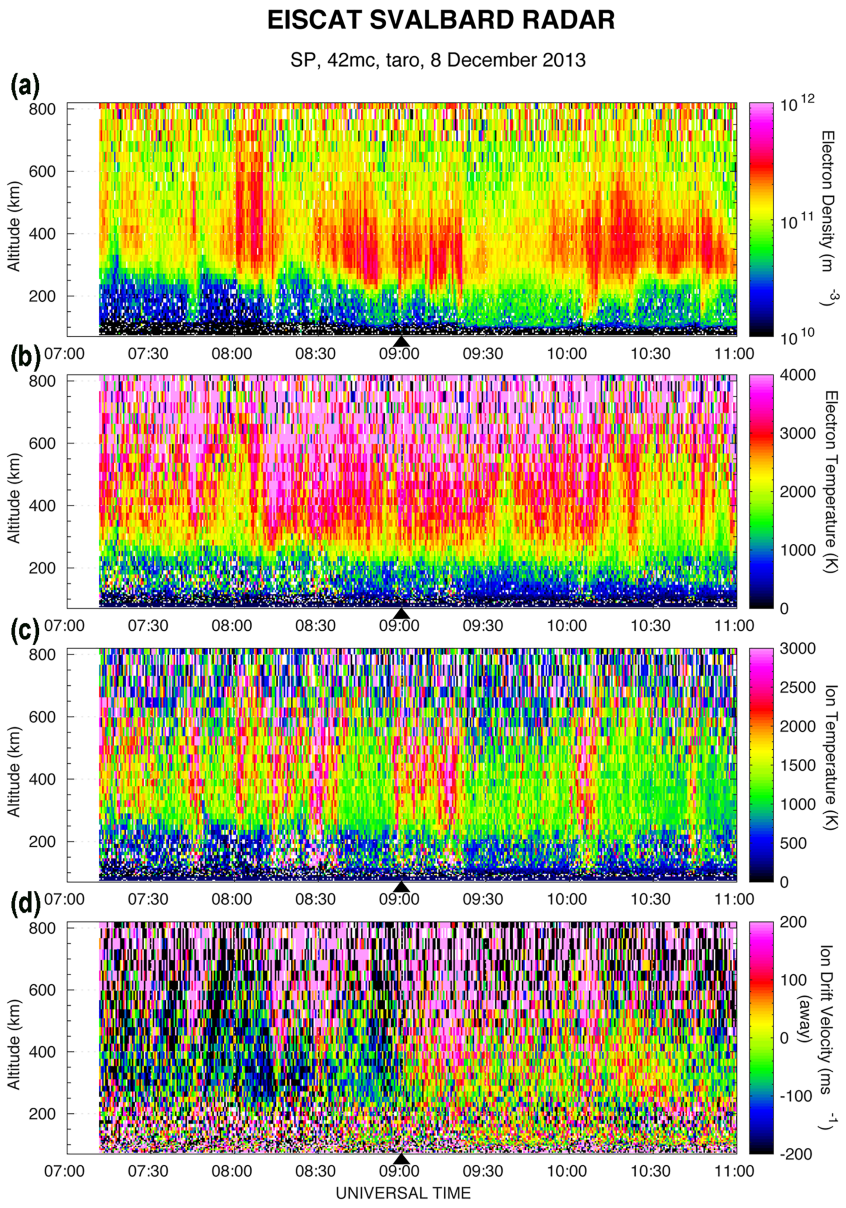

Figure 6. The plasma parameters measured by ESR during 0700–1100 UT. The height profiles of (a) electron density, (b) electron temperature, (c) ion temperature, and (d) field-aligned ion flow velocity are presented. The black triangle indicates the time at which the auroral image shown in Figure 2d was obtained, that is, 0859:47 UT.

4. Discussion

4.1. Ion Flow Pattern

The north-south aligned discrete auroras equatorward of the dayside cusp moved slowly westward, allowing the fixed ESR's field of view to sweep the northern portion of the north-south aligned aurora. The ESR observed T_i enhancements when the ESR's field of view was in the vicinity of the westward boundary of the north-south aligned aurora. A few minutes later, the ESR also observed high T_i when the ESR's field of view was in the vicinity of its eastward boundary.

An enhanced T_i at F region heights is collocated with fast ion flow. This can be explained by the following relationship, based on frictional interactions associated with relative ion-neutral motion (e.g., St. Maurice & Hanson, 1982):

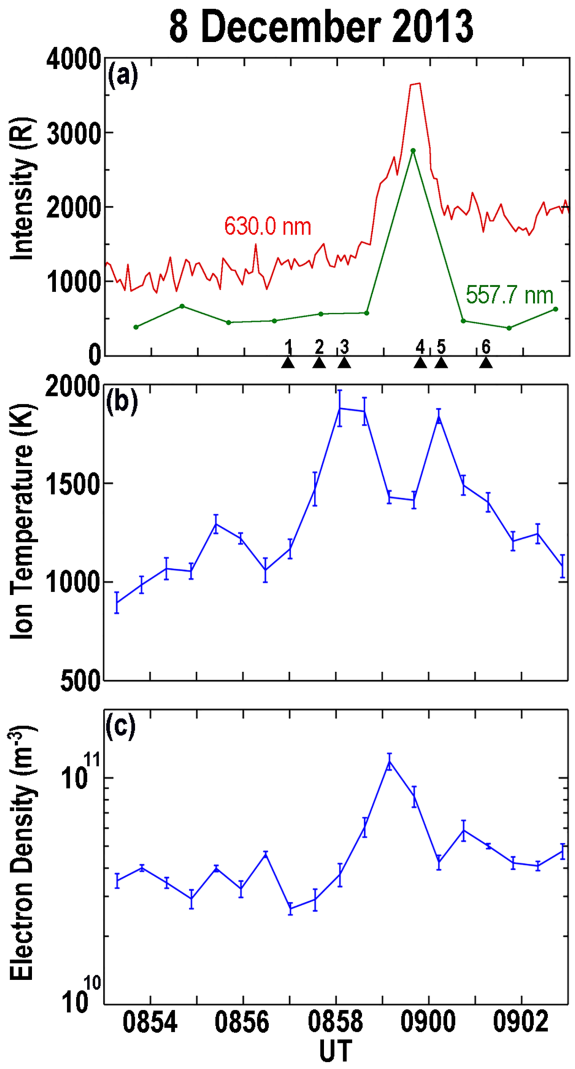

Figure 7. (a) Auroral intensities obtained in the direction of the ESR fixed beam, (b) ESR ion temperatures, and (c) electron density during 0853–0903 UT. The red and green lines in Figure 7a show the variations in the auroral intensities at 630.0-nm and 557.7-nm wavelengths, respectively. The six black triangles indicate 0856:56, 0857:36, 0858:09, 0859:47, 0900:14, and 0901:13 UT. The ion temperature in Figure 7b is the average value from 200 to 350 km, and the electron density in Figure 7c is the average from 150 to 200 km. The error bar is plotted as plus or minus 1 standard deviation of mean value.

$$T_i = T_n + \left(\frac{m_n}{3k_B}\right)|\boldsymbol{v}_i - \boldsymbol{v}_n|^2 \quad (1)$$

where T_i and T_n are the ion and neutral temperatures, respectively, k_B is the Boltzmann constant, $\boldsymbol{v}_i$, and $\boldsymbol{v}_n$ are the horizontal ion and neutral velocities, respectively, and m_n is the collision-frequency-weighted average neutral mass. Under the assumption that the neutral velocity did not change substantially, we consider that enhanced ion flow existed near the north-south aligned auroral structures.

Previous studies have shown that transient flow enhancements sometimes occur on the equatorward side of the cusp (e.g., Lockwood & Carlson, 1992; Taguchi et al., 2010). However, in the present event, the north-south aligned auroral structures existed before the T_i enhancements were observed (Figure 8a; at Time 1) and there was no auroral brightening in the cusp at Time 3 (Figure 8c) or Time 5 (Figure 8e) when the T_i enhancements were observed by the ESR. This implies that the T_i enhancements observed by the ESR were not a result of transient flow enhancements but were rather related to quasi-stable fast flow, which already existed at Time 1. Although we cannot definitively rule out the possibility that the first transient flow enhancement occurred exactly when the ESR's field of view was in the vicinity of the westward boundary of the north-south aligned aurora and that the second flow enhancement also happened exactly when the ESR's field of view was in the vicinity of its eastward boundary, we consider below how a quasi-stable flow pattern can explain the variations in the auroral intensity and T_i in the fixed direction.

The north-south aligned discrete auroras equatorward of the dayside cusp are similar to the Sun-aligned arcs in the polar cap, that is, both are highly elongated aurora arcs. The flow pattern for the Sun-aligned arcs in the polar cap has a flow reversal in the aurora; moreover, the ion flow or horizontal electric field, which produces the flow, has a relatively large magnitude near the westward and eastward boundaries of the aurora (e.g., Frank et al., 1986, their Figure 5). If this flow pattern existed near the present north-south aligned aurora, flow having a southward component should be observed near the north-south aligned aurora, in addition to flow having a northward component. However, such flow was not observed by SuperDARN (Figure 3b).

Figure 9 illustrates a possible flow pattern that does not have a flow reversal. The flow is fast near the eastward and westward boundaries of the north-south aligned aurora and slow in the middle region, coincident with the most enhanced auroral emissions. Considering that the whole flow distribution and the auroral region move westward and pass through a fixed point, the flow variations seen at this fixed point can qualitatively explain the observed ESR T_i variations (Figure 7b).

4.2. Slow-Flow Region

For the plasma flow depression coincident with the auroral arc, a similar tendency has been previously identified in observations made premidnight (e.g., Evans et al., 1977; Wescott et al., 1969), near midnight (e.g., Maynard et al., 1973; Potter, 1970; Whalen et al., 1975), and postmidnight (e.g., Hosokawa et al., 2010; Juusola et al., 2016). The present study has shown that this tendency can also occur in the noon sector.

When a north-south aligned region of electron precipitation causes a channel of high conductivity and the channel is aligned with the plasma flow, the electric field responsible for the flow drives Pedersen currents across the intense electron precipitation and a secondary polarization electric field is created in the direction

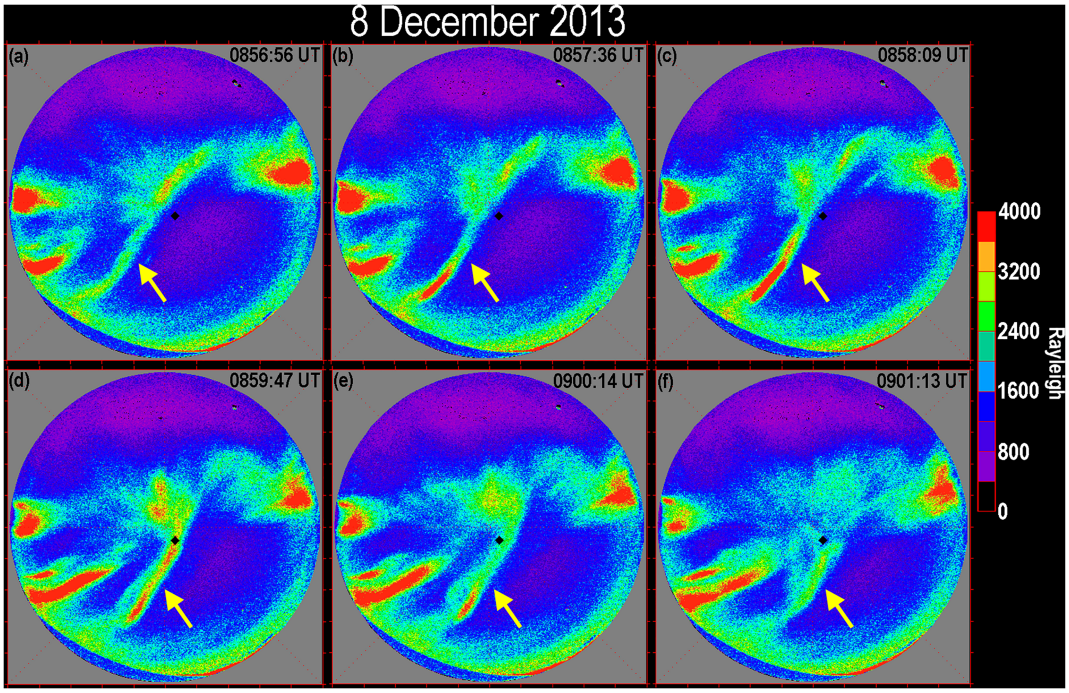

Figure 8. All-sky images (630.0 nm) obtained at Times 1 to 6 of Figure 7a. The format of each image is the same as that of the image shown in Figure 2d. The yellow arrow indicates the north-south aligned auroral structures.

opposite to the primary electric field. The electric field inside the increased conductivity region is reduced in magnitude according to

$$E_{\mathrm{in}} = E_{\mathrm{out}} \frac{\Sigma_{P,\mathrm{out}}}{\Sigma_{P,\mathrm{in}}} \tag{2}$$

where E_{in} and E_{out} are the electric field inside and outside the increased conductivity region, respectively, and $\Sigma_{\mathrm{P,\ in}}$ and $\Sigma_{\mathrm{P,\ out}}$ are the corresponding height-integrated Pedersen conductivities (Paschmann et al., 2002). We note that in the assumed geometry, the Hall current does not have a component normal to the boundary of the increased conductivity region; therefore, the polarization effect due to this current may not be considered. We interpret below the suppressed flow using equation (2).

Figure 10 shows the height profiles of the Pederson conductivity, σ_{P}, based on observations of the ESR electron density and the height-integrated value of those profiles, that is, five height-integrated Pedersen conductivities, Σ_{P}, around the suppressed flow. We applied the height profile of the ESR electron density, n_{e}, to the following relation for two heavy ion species ($j = 1$ and 2 for NO^+ and $O_2{}^+$, respectively):

$$\sigma_P \simeq \frac{n_e e}{B} \sum_{j=1,2} \alpha_j \frac{\Omega_i^j \nu_{\mathrm{in}}^j}{\Omega_i^{j2} + \nu_{\mathrm{in}}^{j2}} \tag{3}$$

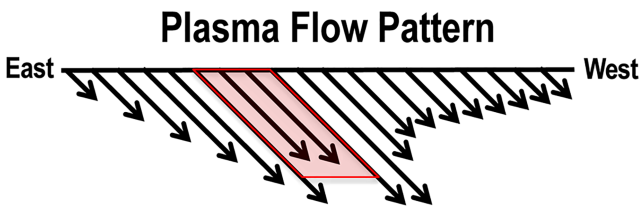

Figure 9. Illustration showing the inferred ion flow pattern. The black arrow represents the magnitude of the flow speed, and the red region indicates the east-west width of the north-south aligned aurora.

where e is the elementary charge in units of C; B is the Earth's magnetic field, which we assume to be 5.7×10^{-5} T; Ω_i^j represents the ion gyrofrequencies of NO^+ and $O_2{}^+$ in Hz; ν_{in}^j is the ion-neutral collision frequency between each ion species and neutral species in Hz; and α_j is the relative abundance of NO^+ and $O_2{}^+$. For the height profiles of relative abundance, we used the International Reference Ionosphere (Bilitza, 2001). We also used the height profiles of the densities of N_2, O_2, and O from the NRLMSISE-00 neutral atmospheric model (Picone et al., 2002) to estimate the ion-neutral collision frequencies, which are represented by the following formulas (Schunk & Walker, 1973):

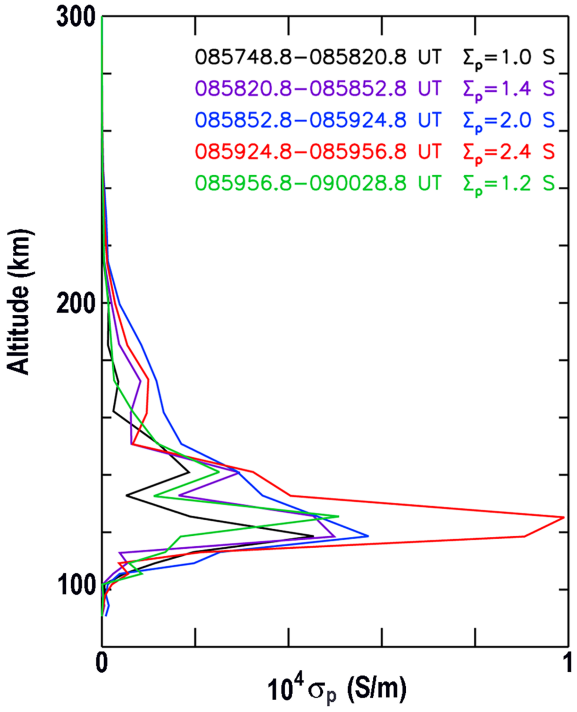

Figure 10. Height profile of the Pedersen conductivities, σ_P, calculated using the ESR electron density observations. The height-integrated Pedersen conductivities, Σ_P are also shown.

$$\nu^1{}_{\rm in} = 4.34\times10^{-16}\, n(N_2) + 4.28\times10^{-16}\, n(O_2) + 2.44\times10^{-16}\, n(O) \quad (4)$$

$$\nu^2{}_{\rm in} = 4.13\times10^{-16}\, n(N_2) + 4.08\times10^{-16}\, n(O_2) + 2.31\times10^{-16}\, n(O) \quad (5)$$

where $n(N_2)$, $n(O_2)$, and $n(O)$ are the densities of N_2, O_2, and O in m^{-3}, respectively.

At 0859:24.8–0859:56.8 UT (red in Figure 10), σ_p is clearly enhanced. At one prior time bin (0858:52.8–0859:24.8 UT, shown in blue), σ_p is relatively large at ~150 to ~200 km. The Σ_P values at these two times are higher than those at the other three times, which is consistent with the electron density variations shown in Figure 7c.

We interpret the ion temperature change ΔT_i as the difference between the ion temperature in the increased conductivity region and that in its adjacent outer region, that is,

$$\begin{aligned} T_i &= T_{i,\rm in} - T_{i,\rm out} \\ &= T_{n,\rm in} - T_{n,\rm out} + \left(\frac{m_n}{3k_B}\right)\left(\left|\boldsymbol{v}_{i,\rm in} - \boldsymbol{v}_{n,\rm in}\right|^2 - \left|\boldsymbol{v}_{i,\rm out} - \boldsymbol{v}_{n,\rm out}\right|^2\right) \end{aligned} \quad (6)$$

When we assume that $\boldsymbol{v}_{i,\rm in}$, $\boldsymbol{v}_{i,\rm out}$, $\boldsymbol{v}_{n,\rm in}$, and $\boldsymbol{v}_{n,\rm out}$ are in the same direction, and that the neutral quantities do not change significantly across the boundary, that is, $T_{n,\rm in} \sim T_{n,\rm out}$ and $\boldsymbol{v}_{n,\rm in} \sim \boldsymbol{v}_{n,\rm out}$, we can reduce equation (6) to

$$T_i \geq \left(\frac{m_n}{3k_B}\right)\left|\boldsymbol{v}_{i,\rm out}\right|^2\left(\frac{\left|\boldsymbol{v}_{i,\rm in}\right|^2}{\left|\boldsymbol{v}_{i,\rm out}\right|^2} - 1\right) = \left(\frac{m_n}{3k_B}\right)\left|\boldsymbol{v}_{i,\rm out}\right|^2\left\{\left(\frac{\Sigma_{P,\rm out}}{\Sigma_{P,\rm in}}\right)^2 - 1\right\} \quad (7)$$

In the inequality of (7), we used $|\boldsymbol{v}_{i,\rm in}| < |\boldsymbol{v}_{i,\rm out}|$. We also used equation (2) in the equality of (7).

For m_n, we assume that the neutral gas in the F region consists of atomic oxygen. When we set $\Sigma_{P,\rm out}$ and $\Sigma_{P,\rm in}$ to 1.0 S and 2.4 S (Figure 10), respectively, equation (7) is reduced to

$$T_i \geq -540\left|\boldsymbol{v}_{i,\rm out}\right|^2 \text{ K} \quad (8)$$

Here, $\boldsymbol{v}_{i,\rm out}$ is given in units of km/s. The SuperDARN data indicate that the maximum plasma flow velocity is approximately 0.7 km/s (Figure 3b). Since there is a tendency for SuperDARN velocities to be roughly 0.7 times larger than ion velocities observed by spacecraft (Drayton et al., 2005), 1 km/s would be a more appropriate value of $|\boldsymbol{v}_{i,\rm out}|$. Equation (8) shows that the depression of T_i is at most 540 K for $|\boldsymbol{v}_{i,\rm out}| = 1$ km/s. This ion temperature depression value is in good agreement with the ESR observation (Figure 7b). When a channel of high conductivity is slightly tilted from the direction of ion flow, the direction of the created polarization electric field would also be tilted slightly from the opposite direction of the primary electric field. The magnitude of the total reduced electric field in the increased conductivity region for this case would be somewhat larger than that for the no-tilt case. In other words, in equation (2) the left-hand side is somewhat larger than the right-hand side, and the equality of (7) would change accordingly. However, this change does not affect the inequality of (8). The observed T_i depression can be understood as the polarization effect owing to the increased conductivity. We note, however, that this interpretation is reasonable when we assume that the whole flow distribution moves westward, as mentioned above. Further study is needed to understand the reasons why the whole flow distribution moves westward.

4.3. Magnetospheric Sources

We have suggested that the north-south aligned auroral structures were in the region of the closed magnetic field lines. We have also suggested that the ion flow region, in which the north-south aligned auroral structures were embedded, moved slowly westward. Figure 11 illustrates the magnetospheric source of the north-south aligned aurora. Since similar auroras existed on the eastward side of the north-south aligned

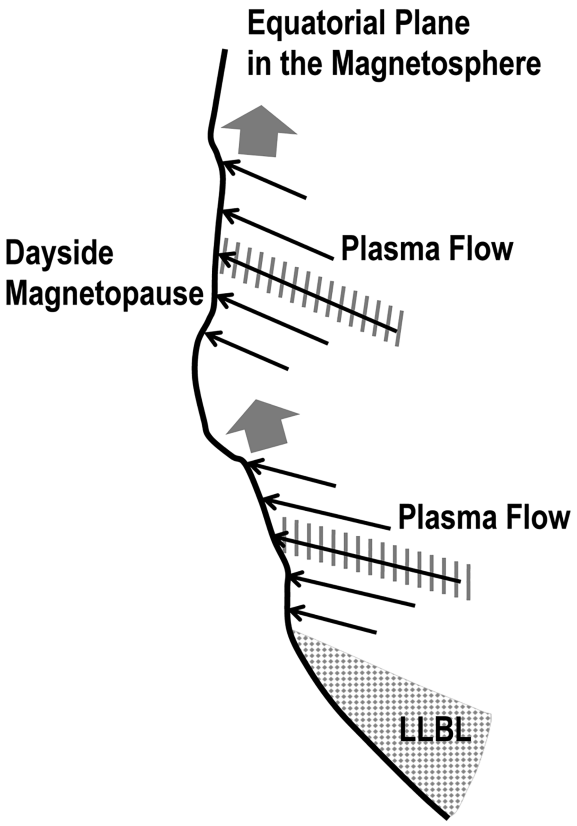

Figure 11. Illustration showing the magnetospheric source of the north-south aligned discrete auroras. The thin black arrows represent that the plasma flows toward the dayside magnetopause. Hatches on the black arrows represent a limited region where enhanced electron precipitation can be caused. The bold gray arrows indicate the direction of the westward shift of the source region. The gray dotted region represents a part of the low-latitude boundary layer (LLBL).

aurora of interest (Figure 2 or Figure 8), we show two source regions in the illustration. Each source region shifts to the west (upward in Figure 11) over time. In each region, plasma flows toward the dayside magnetopause (black arrows). We do not discuss the detailed distribution of plasma flow that might have been modulated by the reduced electric field in the ionosphere. Hatches on the black arrows represent a limited area of the flow region. We can infer that favorable plasma conditions for the formation of the parallel potential drop along the magnetic field lines are satisfied in these limited areas. Moreover, we can infer that the enhanced energy flux of the electrons, which is due to the formed potential drop, causes relatively high conductivity in the ionosphere. These favorable plasma conditions may be associated with suprathermal electron distribution in the magnetosphere, as noted by Dors and Kletzing (1999); however, further study is needed to clarify why those plasma conditions are satisfied in the limited areas embedded in the plasma flow region.

The LLBL is also illustrated in Figure 11 (shaded region). Possible plasma flow in the LLBL occurs away from the subsolar region. The ionospheric counterpart of this kind of plasma flow would be flow that occurs away from the footprint of the near-noon magnetopause, that is, flow toward the later local time (or the earlier local time) in the postnoon (or prenoon) sector. We have shown in Figure 3a that relatively strong auroras are located immediately equatorward of 76 MLAT after ~1300 MLT. We believe that these auroras occur along the magnetic field lines threading the LLBL.

4.4. Comparison With Previous Studies

Two previous studies extensively examined auroral structures similar to those presented in this study by analyzing large data sets from an all-sky imager at Svalbard. Rodriguez et al. (2012) reported that north-south aligned auroral structures were identified on 25 out of 57 days for which (i) the set of all-sky images was complete between 0730 and 1030 UT and (ii) observation conditions were clear during this period. A 43% chance of north-south aligned auroral structures suggests that the appearance of these auroral structures is not unusual, as noted by the authors of that study. However, the north-south aligned auroral structures in the present study differ from the majority of auroral events examined by Rodriguez et al. (2012). In Rodriguez et al. (2012), the auroral structures tended to grow equatorward outward from, and fading back into, the persistent midday aurora. The auroral structures in the present paper did not show such signatures. At the earlier stage, the auroral structures existed in the postnoon sector and then took a stable north-south aligned form after moving westward.

Conducting an extensive survey of dayside auroras, Han et al. (2015) showed that diffuse auroras appear with a striped structure equatorward of the cusp (in addition to the discrete aurora structure shown by Rodriguez et al., 2012). The diffuse aurora had a lower intensity than the north-south aligned auroral structures in the present study; however, the statistical characteristics of the alignment of the diffuse aurora are in good agreement with the features in our event (Figure 8). The auroral structures are nearly parallel to the northwest-southeast direction in the postnoon sector, and in the near-noon sector the auroral structures were nearly parallel to the north-south direction.

5. Conclusions

We have shown the characteristics of north-south aligned discrete auroras in the noon sector on 8 December 2013, focusing on the spatial relationship between the auroral structures and ion flow. North-south aligned discrete auroras were observed during a moderately disturbed period. IMF B_Z was small and negative, and the solar wind dynamic pressure was about 2 nPa. The north-south aligned aurora occurred at 73 to 75

MLAT. The plasma convection, in which the north-south aligned auroral structures were embedded, had northward components and was almost parallel to the north-south aligned aurora. On the prenoon side, a clear convection reversal was observed at ~76 MLAT. This indicates that the north-south aligned auroras, which were observed at 73–75 MLAT, occur in the region of the closed magnetic field line. The ratio of the 557.7-nm intensity to the 630.0-nm intensity in the field-aligned direction, together with the electron density enhancements at relatively low altitudes, also suggest that the north-south aligned aurora occurs in the closed magnetic field lines.

The auroral structures moved slowly westward, allowing the fixed ESR's field of view to sweep the east-west dimension of the northern portion of the auroral structures. Near the eastward and westward boundaries of the northern portion of the auroral structures, the ion flow was relatively fast and the flow enhancements were suppressed in the middle of the auroral structures. This slow-flow region can be interpreted as the electric field being reduced due to the increased Pedersen conductivity. It thus appears that the magnetospheric source is a limited area embedded in the region of plasma flow toward the dayside magnetopause.

Acknowledgments

We would like to thank T. Aoki of University of Electro-Communications for his maintenance of the all-sky imager. We also thank F. Sigernes and M. Syrjäsuo for their help at the University Centre in Svalbard, Longyearbyen. We also thank Y. Oda of Kyoto University for his assistance with DMSP data analyses. The all-sky imager data used in this study can be accessed from this site (http://step0ku.kugi.kyoto-u.ac.jp/data/svalbard/asi/20131208/). EISCAT data can be accessed through the EISCAT website (https://www.eiscat.se/schedule/schedule.cgi). We are indebted to the director and staff of EISCAT for operating the facility and supplying the data. EISCAT is an international association supported by research organizations in China, Finland Japan, Norway, Sweden, and the United Kingdom. The SuperDARN data can be accessed from this site (http://polaris.nipr.ac.jp/~SD/sdjapan/data.html). We acknowledge the use of SuperDARN data. SuperDARN is a collection of radars funded by national scientific funding agencies of Australia, Canada, China, France, Japan, South Africa, United Kingdom, and United States of America. ACE data were obtained through NASA/CDAWeb (http://cdaweb.sci.gsfc.nasa.gov/index.html/). DMSP F16 data were obtained through NOAA Satellite Data Services (https://satdat.ngdc.noaa.gov/dmsp/data/f16/). The *SYM-H* index and *AL* index were provided by the Data Analysis Center for Geomagnetism and Space Magnetism, Kyoto University (http://wdc.kugi.kyoto-u.ac.jp/wdc/Sec3.html). This work was supported by JSPS KAKENHI Grants 22340143 and 26302006. The work by S. T. is also supported by JSPS KAKENHI Grant 15K05300, the Kyoto University Foundation, and ISHIZUE 2019 of Kyoto University Research Development Program.

References

Araki, T. A. (1994). A physical model of geomagnetic sudden commencement. In M. J. Engebretson, K. Takahashi, & M. Scholer (Eds.), *Solar Wind Sources of Magnetospheric Ultra-Low-Frequency Waves*, *Geophys. Monogr. Ser* (Vol. 81, pp. 183–200). Washington, DC: AGU.

Baker, K. B., & Wing, S. (1989). A new magnetic coordinate system for conjugate studies at high latitudes. *Journal of Geophysical Research*, *94*(A7), 9139–9143. https://doi.org/10.1029/JA094iA07p09139

Bilitza, D. (2001). International Reference Ionosphere 2000. *Radio Science*, *36*(2), 261–275. https://doi.org/10.1029/2000RS002432

Chen, X.-C., Han, D.-S., Lorentzen, D. A., Oksavik, K., Moen, J. I., & Baddeley, L. J. (2017). Dynamic properties of throat aurora revealed by simultaneous ground and satellite observations. *Journal of Geophysical Research: Space Physics*, *122*, 3469–3486. https://doi.org/10.1002/2016JA023033

Dandekar, B. S., & Pike, C. P. (1978). The midday, discrete auroral gap. *Journal of Geophysical Research*, *83*(A9), 4227–4236. https://doi.org/10.1029/JA083iA09p04227

Dors, E. E., & Kletzing, C. A. (1999). Effects of suprathermal tails on auroral electrodynamics. *Journal of Geophysical Research*, *104*(A4), 6783–6796. https://doi.org/10.1029/1998JA900135

Drayton, R. A., Koustov, A. V., Hairston, M. R., & Villain, J. P. (2005). Comparison of DMSP cross-track ion drifts and SuperDARN line-of-sight velocities. *Annales de Geophysique*, *23*, 2479–2486. https://doi.org/10.5194/angeo-23-2479-2005

Elphinstone, R. D., Hearn, D. J., Murphree, J. S., Cogger, L. L., Johnson, M. L., & Vo, H. B. (1993). Some UV dayside auroral morphologies. In R. L. Lysak (Ed.), *Auroral Plasma Dynamics*, *Geophys. Monogr. Ser* (Vol. 80, pp. 31–45). Washington, DC: AGU.

Evans, D. S., Maynard, N. C., Trøim, J., Jacobsen, T., & Egeland, A. (1977). Auroral vector electric field and particle comparisons, 2, Electrodynamics of an arc. *Journal of Geophysical Research*, *82*(16), 2235–2249. https://doi.org/10.1029/JA082i016p02235

Fasel, G. J. (1995). Dayside poleward moving auroral forms: A statistical study. *Journal of Geophysical Research*, *100*(A7), 11,891–11,905. https://doi.org/10.1029/95JA00854

Frank, L. A., Craven, J. D., Gurnett, D. A., Shawhan, S. D., Weimer, D. R., Burch, J. L., et al. (1986). The theta aurora. *Journal of Geophysical Research*, *91*(A3), 3177–3224. https://doi.org/10.1029/JA091iA03p03177

Frey, H. U. (2007). Localized aurora beyond the auroral oval. *Reviews of Geophysics*, *45*, RG1003. https://doi.org/10.1029/2005RG000174

Frey, H. U., Mende, S. B., Fuselier, S. A., Immel, T. J., & Østgaard, N. (2003). Proton aurora in the cusp during southward IMF. *Journal of Geophysical Research*, *108*(A7), 1277. https://doi.org/10.1029/2003JA009861

Fuselier, S. A., Gary, S. P., Thomsen, M. F., Claflin, E. S., Hubert, B., Sandel, B. R., & Immel, T. (2004). Generation of transient dayside subauroral proton precipitation. *Journal of Geophysical Research*, *109*, A12227. https://doi.org/10.1029/2004JA010393

Greenspan, M., Anderson, P. B., & Pelagatti, J. M. (1986). Characteristics of the thermal plasma monitor (SSIES) for the Defense Meteorological Satellite Program (DMSP) spacecraft S8 through F10 Tech. Rep., AFGL-TR-86-0227, Air Force Geophysical Laboratory, Hanscom Air Force Base, Mass.

Han, D.-S., Chen, X.-C., Liu, J.-J., Qiu, Q., Keika, K., Hu, Z.-J., et al. (2015). An extensive survey of dayside diffuse aurora based on optical observations at Yellow River Station. *Journal of Geophysical Research: Space Physics*, *120*, 7447–7465. https://doi.org/10.1002/2015JA021699

Han, D.-S., Hietala, H., Chen, X.-C., Nishimura, Y., Lyons, L. R., Liu, J.-J., et al. (2017). Observational properties of dayside throat aurora and implications on the possible generation mechanisms. *Journal of Geophysical Research: Space Physics*, *122*, 1853–1870. https://doi.org/10.1002/2016JA023394

Han, D.-S., Nishimura, Y., Lyons, L. R., Hu, H.-Q., & Yang, H.-G. (2016). Throat aurora: The ionospheric signature of magnetosheath particles penetrating into the magnetosphere. *Geophysical Research Letters*, *43*, 1819–1827. https://doi.org/10.1002/2016GL068181

Hosokawa, K., Motoba, T., Yukimatu, A. S., Milan, S. E., Lester, M., Kadokura, A., et al. (2010). Plasma irregularities adjacent to auroral patches in the postmidnight sector. *Journal of Geophysical Research*, *115*, A09303. https://doi.org/10.1029/2010JA015319

Hosokawa, K., Taguchi, S., & Ogawa, Y. (2016a). Edge of polar cap patches. *Journal of Geophysical Research: Space Physics*, *121*, 3410–3420. https://doi.org/10.1002/2015JA021960

Hosokawa, K., Taguchi, S., & Ogawa, Y. (2016b). Periodic creation of polar cap patches from auroral transients in the cusp. *Journal of Geophysical Research: Space Physics*, *121*, 5639–5652. https://doi.org/10.1002/2015JA022221

Hosokawa, K., Taguchi, S., Ogawa, Y., & Aoki, T. (2013). Periodicities of polar cap patches. *Journal of Geophysical Research: Space Physics*, *118*, 447–453. https://doi.org/10.1029/2012JA018165

Hosokawa, K., Taguchi, S., Ogawa, Y., & Sakai, J. (2013). Two-dimensional direct imaging of structuring of polar cap patches. *Journal of Geophysical Research: Space Physics*, *118*, 6536–6543. https://doi.org/10.1002/jgra.50577

Hubert, B., Gerard, J.-C., Fuselier, S. A., & Mende, S. B. (2003). Observation of dayside subauroral proton flashes with the IMAGE-FUV imagers. *Geophysical Research Letters*, *30*(3), 1145. https://doi.org/10.1029/2002GL016464

Iyemori, T., & Rao, D. R. K. (1996). Decay of the Dst field of geomagnetic disturbance after substorm onset and its implication to storm-substorm relation. *Annales de Geophysique*, *14*, 608–618. https://doi.org/10.1007/s00585-996-0608-3

Juusola, L., Archer, W. E., Kauristie, K., Burchill, J. K., Vanhamäki, H., & Aikio, A. T. (2016). Ionospheric conductances and currents of a morning sector auroral arc from Swarm A electric and magnetic field measurements. *Geophysical Research Letters*, *43*, 11,519–11,527. https://doi.org/10.1002/2016GL070248

Liou, K., Newell, P. T., Sotirelis, T., & Meng, C.-I. (2006). Global auroral response to negative pressure impulses. *Geophysical Research Letters*, *33*, L11103. https://doi.org/10.1029/2006GL025933

Liou, K., Wu, C.-C., Lepping, R. P., Newell, P. T., & Meng, C.-I. (2002). Midday sub-auroral patches (MSPs) associated with interplanetary shocks. *Geophysical Research Letters*, *29*(16), 1771. https://doi.org/10.1029/2001GL014182

Lockwood, M., McCrea, I. W., Milan, S. E., Moen, J., Cerisier, J. C., & Thorolfsson, A. (2000). Plasma structure within poleward-moving cusp/cleft auroral transients: EISCAT Svalbard radar observations and an explanation in terms of large local time extent of events. *Annales de Geophysique*, *18*, 1027–1042. https://doi.org/10.1007/s00585-000-1027-5

Lockwood, M. P., & Carlson, H. C. Jr. (1992). Production of polar cap electron density patches by transient magnetopause reconnection. *Geophysical Research Letters*, *19*, 1731–1734. https://doi.org/10.1029/92GL01993

Lockwood, M. P., Sandholt, E., Cowley, S. W. H., & Oguti, T. (1989). Interplanetary magnetic field control of dayside auroral activity and the transfer of momentum across the dayside magnetopause. *Planetary and Space Science*, *37*(11), 1347–1365. https://doi.org/10.1016/0032-0633(89)90106-2

Lorentzen, D. A., & Moen, J. (2000). Auroral proton and electron signatures in the dayside aurora. *Journal of Geophysical Research*, *105*(A6), 12,733–12,745. https://doi.org/10.1029/1999JA900405

Maynard, N. C., Bahnsen, A., Christophersen, P., Egeland, A., & Lundin, R. (1973). An example of anticorrelation of auroral particles and electric fields. *Journal of Geophysical Research*, *78*(19), 3976–3980. https://doi.org/10.1029/JA078i019p03976

Meng, C.-I. (1981). Electron precipitation in the midday auroral oval. *Journal of Geophysical Research*, *86*(A4), 2149–2174. https://doi.org/10.1029/JA086iA04p02149

Meng, C.-I., & Lundin, R. (1986). Auroral morphology of the midday oval. *Journal of Geophysical Research*, *91*(A2), 1572–1584. https://doi.org/10.1029/JA091iA02p01572

Milan, S. E., Lester, M., Cowley, S. W. H., Moen, J., Sandholt, P. E., & Owen, C. J. (1999). Meridian-scanning photometer, coherent HF radar, and magnetometer observations of the cusp: A case study. *Annales de Geophysique*, *17*, 159–172.

Moen, J., Rinne, Y., Carlson, H. C., Oksavik, K., Fujii, R., & Opgenoorth, H. (2008). On the relationship between thin Birkeland current arcs and reversed flow channels in the winter cusp/cleft ionosphere. *Journal of Geophysical Research*, *113*, A09220. https://doi.org/10.1029/2008JA013061

Newell, P. T., Burke, W. J., Sánchez, E. R., Meng, C.-I., Greenspan, M. E., & Clauer, C. R. (1991). The low-latitude boundary layer and the boundary plasma sheet at low altitude: Prenoon precipitation regions and convection reversal boundaries. *Journal of Geophysical Research*, *96*(A12), 21,013–21,023. https://doi.org/10.1029/91JA01818

Newell, P. T., & Meng, C.-I. (1992). Mapping the dayside ionosphere to the magnetosphere according to particle precipitation characteristics. *Geophysical Research Letters*, *19*(6), 609–612. https://doi.org/10.1029/92GL00404

Ogawa, Y., Fujii, R., Buchert, S. C., Nozawa, S., & Ohtani, S. (2003). Simultaneous EISCAT Svalbard radar and DMSP observations of ion upflow in the dayside polar ionosphere. *Journal of Geophysical Research*, *108*(A3), 1101. https://doi.org/10.1029/2002JA009590

Oksavik, K., Moen, J., & Carlson, H. C. (2004). High-resolution observations of the small-scale flow pattern associated with a poleward moving auroral form in the cusp. *Geophysical Research Letters*, *31*, L11807. https://doi.org/10.1029/2004GL019838

Paschmann, G., Haaland, S., & Treumann, R. (2002). Auroral plasma physics. *Space Science Reviews*, *103*, 41. https://doi.org/10.1023/A:1023030716698

Picone, J. M., Hedin, A. E., Drob, D. P., & Aikin, A. C. (2002). NRLMSISE-00 empirical model of the atmosphere: Statistical comparisons and scientific issues. *Journal of Geophysical Research*, *107*(A12), 1468. https://doi.org/10.1029/2002JA009430

Potter, W. E. (1970). Rocket measurements of auroral electric and magnetic fields. *Journal of Geophysical Research*, *75*(28), 5415–5431. https://doi.org/10.1029/JA075i028p05415

Rodriguez, J. V., Carlson, H. C., & Heelis, R. A. (2012). Auroral forms that extend equatorward from the persistent midday aurora during geomagnetically quiet periods. *Journal of Atmospheric and Solar - Terrestrial Physics*, *86*, 6–24. https://doi.org/10.1016/j.jastp.2012.06.001

Sakai, J., Hosokawa, K., Taguchi, S., & Ogawa, Y. (2014). Storm-time enhancements of 630.0-nm airglow associated with polar cap patches. *Journal of Geophysical Research: Space Physics*, *119*, 2214–2228. https://doi.org/10.1002/2013JA019197

Sandholt, P. E., Deehr, C. S., Egeland, A., Lybekk, B., Viereck, R., & Romick, G. J. (1986). Signatures in the dayside aurora of plasma transfer from the magnetosheath. *Journal of Geophysical Research*, *91*(A9), 10,063–10,079. https://doi.org/10.1029/JA091iA09p10063

Sandholt, P. E., & Farrugia, C. J. (2003). Does the aurora provide evidence for the occurrence of antiparallel magnetopause reconnection? *Journal of Geophysical Research*, *108*(A12), 1466. https://doi.org/10.1029/2003JA010066

Schunk, R. W., & Walker, J. C. G. (1973). Theoretical ion densities in the lower ionosphere. *Planetary and Space Science*, *21*(11), 1875–1896. https://doi.org/10.1016/0032-0633(73)90118-9

Shepherd, G. G., Thirkettle, F. W., & Anger, C. D. (1976). Topside optical view of the dayside cleft aurora. *Planetary and Space Science*, *24*, 937–944. https://doi.org/10.1016/0032-0633(76)90004-0

Sipler, D. P., & Biondi, M. A. (1972). Measurements of O(^{1}D) quenching rates in the *F* region. *Journal of Geophysical Research*, *77*(31), 6202–6212. https://doi.org/10.1029/JA077i031p06202

Skjæveland, Å. S., Carlson, H. C., & Moen, J. I. (2017). A statistical survey of heat input parameters into the cusp thermosphere. *Journal of Geophysical Research: Space Physics*, *122*, 9622–9651. https://doi.org/10.1002/2016JA023594

St. Maurice, J.-P., & Hanson, W. B. (1982). Ion frictional heating at high latitudes and its possible use for an in situ determination of neutral thermospheric winds and temperatures. *Journal of Geophysical Research*, *87*(A9), 7580–7602. https://doi.org/10.1029/JA087iA09p07580

Taguchi, S., Chiba, Y., Hosokawa, K., & Ogawa, Y. (2017). Horizontal profile of a moving red line cusp aurora. *Journal of Geophysical Research: Space Physics*, *122*, 3509–3525. https://doi.org/10.1002/2016JA023115

Taguchi, S., Hosokawa, K., & Ogawa, Y. (2015a). Investigating the particle precipitation of a moving cusp aurora using simultaneous observations from the ground and space. *Progress in Earth and Planetary Science*, *2*, 11. https://doi.org/10.1186/s40645-015-0044-7

Taguchi, S., Hosokawa, K., & Ogawa, Y. (2015b). Three-dimensional imaging of the plasma parameters of a moving cusp aurora. *Journal of Atmospheric and Solar-Terrestrial Physics*, *133*, 98–110. https://doi.org/10.1016/j.jastp.2015.08.012

Taguchi, S., Hosokawa, K., Ogawa, Y., Aoki, T., & Taguchi, M. (2012). Double bursts inside a poleward-moving auroral form in the cusp. *Journal of Geophysical Research*, *117*, A12301. https://doi.org/10.1029/2012JA018150

Taguchi, S., Hosokawa, K., Suzuki, S., Tawara, A., Frey, H. U., Matzka, J., et al. (2010). Plasma flow during the brightening of proton aurora in the cusp. *Journal of Geophysical Research*, *115*, A10308. https://doi.org/10.1029/2010JA015535

Wescott, E. M., Stolarik, J. D., & Heppner, J. P. (1969). Electric fields in the vicinity of auroral forms from motions of barium vapor releases. *Journal of Geophysical Research*, *74*(14), 3469–3487. https://doi.org/10.1029/JA074i014p03469

Whalen, B. A., Verschell, H. J., & McDiarmid, I. B. (1975). Correlations of ionospheric electric fields and energetic particle precipitation. *Journal of Geophysical Research*, *80*(16), 2137–2145. https://doi.org/10.1029/JA080i016p02137

Zhang, Y., & Paxton, L. J. (2006). Dayside convection aligned auroral arcs. *Geophysical Research Letters*, *33*, L13107. https://doi.org/10.1029/2006GL026388

Zhang, Y., Paxton, L. J., Immel, T. J., Frey, H. U., & Mende, S. B. (2002). Sudden solar wind dynamic pressure enhancements and dayside detached auroras: IMAGE and DMSP observations. *Journal of Geophysical Research*, *107*(A4), 8001. https://doi.org/10.1029/2002JA009355

Zhang, Y., Paxton, L. J., Meng, C.-I., Morrison, D., Wolven, B., Kil, H., & Christensen, A. B. (2004). Double dayside detached auroras: TIMED/GUVI observations. *Geophysical Research Letters*, *31*, L10801. https://doi.org/10.1029/2003GL018949

Zhou, X., & Tsurutani, B. T. (1999). Rapid intensification and propagation of the dayside aurora: Large scale interplanetary pressure pulses (fast shocks). *Geophysical Research Letters*, *26*(8), 1097–1100. https://doi.org/10.1029/1999GL900173